

**NASA  
Technical  
Paper  
2374**

November 1984

**Flight and Wind-Tunnel  
Comparisons of the  
Inlet/Airframe Interaction  
of the F-15 Airplane**

Lannie D. Webb,  
Dom Andriyich-Varda,  
and Stephen A. Whitmore



1984

# Flight and Wind-Tunnel Comparisons of the Inlet/Airframe Interaction of the F-15 Airplane

Lannie D. Webb,  
Dom Andriyich-Varda,  
and Stephen A. Whitmore

*Ames Research Center  
Dryden Flight Research Facility  
Edwards, California*



National Aeronautics  
and Space Administration

Scientific and Technical  
Information Branch

## SUMMARY

The design of inlets and nozzles and their interactions with the airplane may account for a large percentage of the total drag of modern high-performance aircraft. This paper describes the inlet/airframe interactions program and the flight tests conducted at the Dryden Flight Research Facility of the NASA Ames Research Center. Inlet-drag and lift data from a 7.5-percent-scale wind-tunnel model are compared with data from an F-15 airplane with instrumentation to match the model. Pressure coefficient variations with variable cowl angles, capture ratios, and angles of attack are examples of flow interactions presented. Data are presented for Mach numbers of 0.6, 0.9, 1.2, and 1.5.

## INTRODUCTION

As the effort to optimize aircraft performance over an increasingly larger flight region continues, more complicated flight configurations evolve. Flow interactions of the inlets, nozzles, and airframe can change the aircraft's stability and trim drag, and in conjunction with other factors, can result in increased total aircraft drag. The need to understand the effects of these interactions on high-performance aircraft having complex external design characteristics has precipitated a wave of testing and analysis (ref. 1). These studies could do two things: point to new drag determination methods, and aid in the design of more energy-efficient aircraft.

To gather data for use with flow interactive studies, a flight research program cosponsored by NASA and the U.S. Air Force was conducted at the Dryden Flight Research Facility of the NASA Ames Research Center (ARC), using an F-15 airplane (fig. 1). The program was designed to compare flight and wind-tunnel data for inlet/airframe interactions and to produce a data base for future study. The wind-tunnel data were obtained from tests conducted in the 14-Foot Transonic Wind Tunnel at the NASA Ames Research Center (ref. 2). Follow-on tests were conducted by the Air Force Flight Dynamics Laboratory and the McDonnell Douglas Corporation in the Arnold Engineering Development Center (AEDC) 16-Foot Transonic Wind Tunnel (ref. 3.)

This report discusses in detail the NASA Ames Dryden inlet/airframe interaction program, which was part of a larger program to study nozzle-airframe interactions (ref. 4) and to perform an extensive engine calibration test (ref. 5). The test conditions and the instrumentation on both the model and the aircraft are described. Flight and wind-tunnel inlet drag data, derived by pressure integration equations, are compared. These, in turn, are compared with the inlet drag measured by a force balance on the wind-tunnel model (fig. 2). The effects of angle of attack, varying capture ratios, a movable cowl, and other system components on pressure flow fields along the airframe are discussed.

## NOMENCLATURE

- A            inlet capture as a function of  $\rho$  and  $\alpha$ ,  $m^2$  (ft<sup>2</sup>)
- A<sub>C</sub>          inlet capture area  $\alpha = 0^\circ$  as a function of  $\rho$ ,  $m^2$  (ft<sup>2</sup>)

$A_{CO}$	inlet capture area $\alpha = \rho = 0^\circ$ , $m^2$ (ft <sup>2</sup> )
$A_O$	total inlet captured stream-tube area including duct and bleed flow, $m^2$ (ft <sup>2</sup> )
$A_O/A$	mass flow ratio referenced to inlet capture area as a function of $\rho$ and $\alpha$
$A_O/A_C$	mass flow ratio referenced to inlet capture area $\alpha = 0^\circ$ as a function of $\rho$
$A_O/A_{CO}$	mass flow ratio referenced to inlet capture area at $\alpha = \rho = 0^\circ$
$A_I$	inlet throat capture area, $m^2$ (ft <sup>2</sup> )
$C_p$	pressure coefficient, $\frac{p_m - p_\infty}{q_\infty}$
$C_{Plf}$	lower fuselage pressure coefficient, $\frac{C_{Plf} - p_\infty}{q_\infty}$
$C_{Puf}$	upper fuselage pressure coefficient, $\frac{C_{Puf} - p_\infty}{q_\infty}$
CDIP	inlet drag coefficient
CLIP	inlet lift coefficient
$D_{add}$	additive drag, defined in figure 11(d), N (lb)
$F_{Clx}$	axial force component acting on lower cowl, N (lb)
$F_{Cly}$	normal force component acting on lower cowl, N (lb)
$F_{Cux}$	axial force component acting on upper cowl, N (lb)
$F_{Cuy}$	normal force component acting on upper cowl, N (lb)
$F_I$	stream thrust at left-hand inlet plane section, N (lb)
$F_{ispx}$	axial force component acting on inboard sideplate, N (lb)
$F_{ispy}$	normal force component acting on inboard sideplate, N (lb)
$F_{ospx}$	axial force component acting on outboard sideplate, N (lb)
$F_{ospy}$	normal force component acting on outboard sideplate, N (lb)
$F_O$	free-stream stream thrust, N (lb)

$F_{1r}, F_{2r}, F_{3r}$	forces acting on first, second, and third ramps, respectively, normal to ramp surface, N (lb)
F.S.	fuselage station, cm (in)
$h_{\infty}$	true pressure altitude, m (ft)
L	length from tip of nose to end of tail boom ( $L = 1890.3$ cm (744.21 in)), see figure 8
$L_{add}$	additive lift, defined in figure 11(d), N (lb)
$M_{\infty}$	free-stream Mach number
$P_m$	surface static pressure, $N/m^2$ (lb/ft <sup>2</sup> )
$P_o$	free-stream total pressure, $N/m^2$ (lb/ft <sup>2</sup> )
$P_{\infty}$	free-stream static pressure, $N/m^2$ (lb/ft <sup>2</sup> )
pcm	pulse-code modulation
$q_{\infty}$	free-stream dynamic pressure, $N/cm^2$ (lb/in <sup>2</sup> )
Re	Reynolds number based on length of model or aircraft length
rms	root mean square
$V_o$	free-stream velocity, m/sec (ft/sec)
X	distance measured from tip of aircraft nose, cm (in)
X/L	ratio of distance back from tip of aircraft's nose to L (see fig. 8)
WAT2	corrected engine airflow, kg/sec (lb/sec)
$\alpha$	free-stream angle of attack, deg
$\beta$	free-stream angle of sideslip, deg
$\Delta'_1, \Delta'_2, \Delta'_3$	first, second, and third ramp angles relative to waterline, deg
$\rho$	inlet rotation angle (fig. 3(b))

## DESCRIPTION OF APPARATUS

### Airplane

The F-15 airplane (fig. 3(a)) is a single-seat, high-performance, all-weather superiority fighter aircraft which has performance capabilities at speeds in excess of Mach 2. The airplane has twin vertical stabilizers, horizontal stabilators, a high-mounted swept-back wing, and twin F100-PW-100 afterburning turbofan engines.

The inlet system of the F-15 airplane (fig. 3(b)) consists of two two-dimensional, external compression, horizontal ramp inlets. Each inlet has three ramps mounted in an overhead arrangement that rotates about a transverse hinge point at the lower cowl lip. This arrangement provides for a variable geometric capture area. The second and third ramps, along with the sideplates, are designed with porous bleed holes to remove the lower energy boundary-layer flow. This flow is exhausted through the louvered bleed exits shown in figure 3(c). In addition to the louvered bleed exits, a variable bypass door provides for removal of larger amounts of air. At supersonic speeds, the bypass door is modulated to maintain the proper throat Mach number.

The inlet control system can be operated from one of two modes. In one mode, the rotating cowl, inlet ramps, and bypass door are automatically positioned by the air inlet controller. The second mode used for these tests consisted of a manual inlet control system that permitted the pilot to set the inlet geometry to any desired position.

### Wind-Tunnel Model

The 7.5-percent wind-tunnel model (ref. 2) is both a force and pressure model and is a scaled version of the F-15 airplane. The model has two balances: one to measure forces on the left inlet, and one to measure forces on the entire aircraft (fig. 4). The metric portion of the inlet includes the upper and lower cowls plus both sideplates. The model was supported by two flow-through sting tubes which serve as inlet mass flow tubes.

The inlet system on the wind-tunnel model is shown in detail in figure 5. In addition to the bleed system, movable ramps, and cowl, the inlet has a fixed-throat slot bleed/bypass exit.

### Model-to-Airplane Comparison

For the flight-test program, the airplane was instrumented with pressure orifices on the left side of the fuselage, where much of the needed instrumentation wiring already existed. With the exception of a few additional pressure orifices on the centerline of the lower cowl lip and in the wing root area, the exterior of the left side of the airplane was configured to match the right side of the wind-tunnel model (fig. 6) as closely as possible. To define inlet conditions (ref. 6), three total pressure probes were installed in the inlet and were used in addition to the total pressure probe for the air inlet controller. The airplane's left-hand secondary environmental control system (ECS) was covered with a wedge tip to match the model's boundary-layer diverter. The F-15 airplane has a noseboom pitot-static probe system (fig. 3(a)) and a variable bypass door (fig. 3(b)), both of which the

model lacked. A comparison between the aircraft's and the wind-tunnel model's bleed and bypass systems, which are located on the upper cowl, is shown in figure 7.

Figure 8 is presented to aid in the comparison of model and airplane locations. This figure relates major fuselage stations (used in wind-tunnel reports) to the X/L ratio used in this report.

## INSTRUMENTATION

To obtain the same pressure measurements on the F-15 airplane as on the wind-tunnel model, over 150 static pressure ports were installed for the inlet/airframe interaction program.

Pressure measurement accuracy was increased by controlling the temperature of all pressure transducers and by using a pressure reference system (refs. 6 and 7). All surface ports were monitored by differential pressure transducers having ranges of  $\pm 1.4 \text{ N/cm}^2$  ( $\pm 2 \text{ lb/in}^2$ ),  $\pm 2.8 \text{ N/cm}^2$  ( $\pm 4 \text{ lb/in}^2$ ), and  $\pm 4.1 \text{ N/cm}^2$  ( $\pm 6 \text{ lb/in}^2$ ). Wind-tunnel data were used primarily in the selection of these pressure transducer ranges with two objectives in mind: (1) to minimize pressure measurement error, and (2) to maximize flight envelope coverage. The reference side of these transducers was connected to one of three tanks (high, medium, and low). The absolute pressures in these tanks were measured by precision digital-quartz pressure transducers. The low and medium reference pressure source is a hemispherical probe (ref. 6) located on the right wing fairing. The low reference pressure tank is supplied by four manifolded static orifices located  $90^\circ$  from the stagnation port on the hemispherical sensor, while the medium reference tank is fed by the  $60^\circ$  port. The high reference pressure source is a duct static orifice near the left engine compressor face (ref. 6). The data were recorded digitally using a pulse-code modulation (pcm) system, and were both recorded on board and telemetered to the ground.

## PROCEDURE

### Wind Tunnel Tests

The model was tested in the AEDC 16-Foot Transonic Wind Tunnel to obtain inlet drag, lift, and interaction data for primary Mach numbers of 0.6, 0.9, 1.2, and 1.5, over angles of attack from  $-1^\circ$  to  $17^\circ$ , and at five basic inlet configurations. Effects on the inlet/airframe interaction from inlet rotation angle, second and third ramp angles, inlet bleeds, inlet mass flow ratio, Reynolds number, and horizontal stabilator angle were determined (ref. 3).

### Flight Tests

From the AEDC wind-tunnel conditions tested, certain points were selected that were considered primary for wind-tunnel-to-flight comparisons. The basic conditions were Mach numbers of 0.6, 0.9, 1.2, and 1.5, and angles of attack of  $0^\circ$ ,  $3^\circ$ , and  $5^\circ$ . These conditions were tested with combinations of five cowl angles and three engine power settings to obtain various inlet capture ratios. A complete list of desired test conditions is contained in table 1 of reference 6.

Flight Conditions. - A majority of the primary flight points were flown at an altitude of approximately 6.1 km (20,000 ft), at Mach numbers of 0.6 and 0.9, and angles of attack of 0°, 3°, and 5°. A few flight points were flown at an angle of attack of 8° and an altitude of approximately 10.7 km (35,000 ft).

Two types of maneuvers were performed in obtaining flight-to-wind-tunnel match points. For angles of attack near 0°, a pullup-pushover maneuver was used, whereas for the higher angles of attack, a constant sustained turn was performed.

For most test conditions, three inlet capture ratios (small, medium, and large) were desired. The numerator of the ratio was changed by varying the engine mass flow; the denominator was changed with geometric capture area. The pilot would run the engines asymmetrically with the left power lever angle at either idle, 80 percent, or military power, while the right engine was set to maintain flight conditions. Figure 9 shows engine airflow as a function of Mach number for two engine power settings — idle and military. Over the subsonic Mach number range, a variety of engine airflows are available.

At the higher Mach numbers (1.2 and 1.5), which were flown at approximately 9.1 km (30,000 ft), the rpm lockup limited the airflow range and, hence, the range of capture ratios (fig. 9). An attempt was made at  $M_\infty = 1.2$  to expand the inlet capture ratio by performing level decelerations through  $M_\infty = 1.2$ , at reduced power settings. For the  $M_\infty = 1.5$  test condition, only one airflow is possible, because of the rpm lockup which prevents inlet buzz.

Uplink. - Establishing a flight point to match a particular wind-tunnel condition required more than standard instrumentation and flight techniques (refs. 8 and 9). A special instrument using two sets of nulling cross pointers was added to permit the pilot to fly altitude and angle of attack simultaneously. This instrument operates as follows: Indicated angle of attack and altitude are transmitted (along with other parameters) from the airplane to the control room, where they are computer corrected and compared with values input by the flight controller. The differences between the desired and actual values are then transmitted (uplinked) back to the aircraft display dial. In addition, flight and pressure sensor parameters were displayed in the ground station on strip charts and on cathode ray tube (CRT) displays.

Tolerances. - Immediately following completion of a maneuver, the decision was made whether to repeat the flight point based on a sensitivity analysis of the inlet drag and lift equations. Perturbations of these equations using incremental values of flight parameters showed that inlet drag and lift were quite sensitive to angle of attack and, to a lesser degree, to Mach number and free-stream static pressure (altitude). The study established the following as acceptable tolerances in the flight parameters:

$\alpha$ , deg . . . . .	$\pm 0.25$
$\beta$ , deg . . . . .	$\pm 0.25$
$M_\infty$ . . . . .	$\pm 0.01$

Reynolds Number. - It was not possible to match Reynolds numbers, since the wind-tunnel values were significantly lower than the flight values (fig. 10). Most of the wind-tunnel runs were at the primary Reynolds number of 12 million. The flight Reynolds numbers ranged from 150 million to 280 million.



## DATA ANALYSIS

### Equations Used

Wind-Tunnel Application. - Inlet drag and lift in this report are plotted as a function of the inlet variable capture ratio,  $A_0/A$ . Figure 11(a) shows the relationship of captured stream tube areas to the geometric capture area for the F-15 inlet.

The defining equations for inlet drag are shown in figure 11(b) and are discussed in detail in reference 3. In general, the total inlet drag is the sum of the axial pressure forces acting over the external inlet surfaces (upper and lower cowls, plus inboard and outboard sideplates), plus the pressure force acting on the unbound captured stream tube (additive drag) between the free-stream conditions and the inlet-lip conditions (momentum change).

Figure 11(c) illustrates the relationship of the control volume and inlet. The figure also presents a detailed breakdown of the basic inlet drag and lift equations and gives the relationship of the additive drag and lift terms to these equations. All the components of force are resolved parallel to the local flow conditions by the  $\sin \alpha$  and  $\cos \alpha$  terms.

The additive drag and lift terms are composed of the normal forces on the three ramps, and the free-stream and inlet-plane stream thrust (fig. 11(d)). The free-stream stream thrust ( $F_0$ ) term has eight parts which account for all the possible airflows. The parts of the airflow are engine, five bleeds (second and third ramps, inboard and outboard, and throat slot), bypass door, and leakage.

Flight Application. - The inlet flow equations involve momentum terms, free-stream flow quantities, and pressures. To handle these terms, flight-measured parameters were substituted into the wind-tunnel equations. For example, calibrated engine airflow (ref. 5) was substituted for the wind-tunnel calibrated nozzle airflow. Corrected air-data quantities from the calibrated pitot-static probe on the noseboom were used for free-stream Mach number ( $M_\infty$ ), free-stream static pressure ( $p_\infty$ ), and free-stream total pressure ( $P_0$ ) in the equations. Corrected angle of attack ( $\alpha$ ) and angle of sideslip ( $\beta$ ) were taken from the vanes on the noseboom.

### Data Selection

Flight data are recorded onboard and in the ground station and then are processed on a CDC CYBER 73 computer, at which time all corrections (such as pressure transducer zeros and air-data corrections from indicated to true) are made. The data are run through the wind-tunnel equations to calculate inlet drag and lift. A 10-sec interval of semisteady conditions is then selected to match the wind-tunnel point for angles of attack and sideslip, Mach number, cowl angle, and third ramp angle. For the final data, a 1-sec time point is selected from the 10-sec interval based on sensitivity analysis.

## ACCURACY

Uncertainties in the calculated data were assessed partially on the basis of calibrations of the wind tunnel (ref. 3) and from results of the laboratory calibration of the approximately 150 transducers used to measure surface pressures.

In addition, the accuracy of the air-data parameters, needed to calculate inlet drag and lift, was assessed based on (a) the laboratory calibrations of the air-data transducers and (b) analysis of the data from several dedicated airspeed calibration flights. From these tests and from an error analysis study prepared by McDonnell Aircraft Company for Ames Dryden (see appendix), figure 12 and table 1 were prepared. Figure 12(a) relates uncertainties in the values of  $C_p$  measured on two important areas used to calculate inlet drag and lift (that is, upper and lower cowls), over the flight range of dynamic pressures. The figure shows that the  $C_p$  values derived from flight data approach the  $\pm 0.005$  wind-tunnel accuracy (ref. 3) only for  $q_\infty > 4 \text{ N/cm}^2$  ( $\text{lb/in}^2$ ). In figure 12(b), a  $2\sigma$  uncertainty in inlet drag and lift from flight data (app.) is plotted as a function of  $M_\infty$ . This may be compared to wind-tunnel uncertainties shown in table 1 (ref. 3) and from data from the appendix.

## PRESENTATION OF RESULTS

### Surface-Pressure Distribution

This section of the report illustrates a few selected effects of flow interaction along the left side of the aircraft. Figure 13 shows pressure changes along the upper and lower surfaces of the aircraft at a flight condition where  $M_\infty = 0.9$ ,  $\alpha = 3^\circ$ , and  $\rho = 0^\circ$ . These changes are the result of the varying amounts of spillage air that result from running the engine at the three settings (idle, 80 percent, and military). Large variations in  $C_{p_{lf}}$  as a function of  $X/L$  exist over the forward portion of the lower cowl (fig. 13(a)). Pressure coefficients on the lower cowl lip ( $X/L = 0.402$ ) vary widely with mass flow changes (fig. 13(a)) and also with other parameters (ref. 10). These variations in  $C_{p_{lf}}$  decrease rapidly with increasing  $X/L$  in both the wind-tunnel and flight data. Over the upper surface (fig. 13(b)), less variation with power settings is noted. The variation in  $C_{p_{uf}}$  at  $X/L = 0.476$  results from the fact that the orifice on the aircraft is located just aft of the open bypass door bleed (fig. 7). The location of the metric break on the wind-tunnel model is shown in figure 13 for reference. The trends and the levels of the data are similar to values found at other flight conditions (refs. 6 and 10).

Figure 14 illustrates the variations in  $C_{p_{lf}}$  and  $C_{p_{uf}}$  with  $X/L$  for two cowl angles ( $\rho = 4^\circ$  and  $7^\circ$ ) at  $M_\infty = 0.9$ ,  $\alpha = 3^\circ$ , and a military power engine setting. Starting near the leading edge of the lower cowl lip, values of  $C_{p_{lf}}$  are affected by rotation of the upper cowl (fig. 14(a)). With increasing values of  $X/L$ , the pressures reach a minimum near  $X/L = 0.418$  and then return to near free-stream conditions over most of the lower fuselage. Downstream of the lower cowl area, the effects from cowl rotation are minimal (fig. 14(a) and ref. 10). Near the left-hand nozzle area, the flight-measured pressures became more negative again. On the upper surface (fig. 14(b)), except for the leading-edge orifice ( $X/L = 0.303$ ) and the orifice aft of the bypass door bleed ( $X/L = 0.476$ ), cowl-angle effects were not large. Downstream of the upper cowl the effects of a variable cowl angle were not evident,

except near the left-hand nozzle ( $X/L = 0.878$ ). These effects of cowl angle on pressures in the nozzle area were found to exist almost to the end of the nozzle (ref. 10). As in the previous figure, wind-tunnel and flight data show good agreement in most areas.

Figure 15 illustrates the variations in  $C_{p_{lf}}$  and  $C_{p_{uf}}$  with  $X/L$  for two angles of attack ( $\alpha = 0^\circ$  and  $5^\circ$ ) at  $M_\infty = 0.9$ ,  $\rho = \infty$ , and a military power engine setting. In contrast with the previous figure where the effects of  $\rho$  were not sensed over much of the mid and aft areas of the aircraft (fig. 14), pressures varied with  $\alpha$  over the entire aircraft (figs. 15(a) and (b)). Large variations in pressures were found near the leading edges, while small ones were found to exist near the nozzle. Wind-tunnel and flight data agreed well over much of the range.

In addition to the interaction effects from changes in mass flow (fig. 13), cowl angle (fig. 14), and angle of attack (fig. 15), many other variables can affect pressures around the aircraft. For example, the effects resulting from orifice location or a change in sideslip were examined in reference 6, and reference 10 contains forebody, boundary-layer diverter, and nozzle interaction data. Although other areas of the aircraft could be studied, the data in the previous figures, along with references 3, 6, and 10, present a sizable cross section of results.

#### Inlet Drag and Lift

The preceding analysis of flow-field interactions around the inlet and along the fuselage represented only a part of this study. The other portion consisted of the correlation of flight and wind-tunnel values of inlet drag and lift obtained by pressure integrations. From these comparisons, the feasibility and accuracy of using the pressure integration technique to determine inlet drag and lift from flight data may be assessed. In addition, these comparisons, along with other flight and wind-tunnel studies (refs. 11 and 12), can give insight into spillage-drag effects.

Figure 16 shows the variation of inlet drag (CDIP) and lift (CLIP) as a function of  $A_0/A$  at  $M_\infty = 0.6, 0.9, 1.2$ , and  $1.5$  for  $\rho = 0^\circ$  and  $\Delta'3 = 11.2^\circ$ . Figure 16(a) compares the flight and wind-tunnel calculation of total inlet drag and lift at  $M_\infty = 0.6$  and  $\alpha = 0^\circ$ . The pressure-integrated drags show reasonable agreement with each other and with the force-balance drag for low inlet-capture ratios. At the higher inlet-capture ratio, the pressure-integrated drags differ considerably from the force-balance drag. This anomaly may be the result of inability of the pressure integration technique to account for static pressure or flow angularity gradients in the inlet plane, especially at the lower Mach numbers (ref. 3). The pressure-integrated data were faired for ease of comparison with the force-balance data and the two-dimensional potential flow curve (ref. 3). Inlet lift shows good agreement among all three sources. In figure 16(b), for  $M_\infty = 0.9$ , there is improved agreement among all three sources of inlet drag. This is attributed to the reduced turning of the flow at the increased Mach number. Inlet lift showed more scatter for this condition. Good agreement between flight and wind-tunnel data was found at the supersonic Mach numbers (1.2 and 1.5) for both CDIP and CLIP. For these conditions, only one flight point was possible because of the engine limitations discussed in the PROCEDURE section. In all four parts of this figure, the effects of increased spillage drag with decreasing values of  $A_0/A$  can be noted. A determination of the absolute magnitude of spillage drag is not possible since values of  $A_0/A$  never reached a "no-spill" condition.

Figure 17 shows the variation of CDIP and CLIP with  $M_\infty$  for  $\alpha = 0^\circ$  and  $5^\circ$ , respectively, and for  $\rho = 0^\circ$ . The flight and wind-tunnel data show reasonable agreement, and illustrate increasing inlet drag and lift with increasing  $M_\infty$ . Figure 18 presents the variation of inlet drag (fig. 18(a)) and lift (fig. 18(b)) with  $\alpha$  for  $\rho = 0^\circ$  at  $M_\infty = 0.6$  and  $1.5$ , respectively. Generally good agreement in the drag trends and, to a lesser degree in the lift curves, are noted over the  $\alpha$  range. In figure 19 the variation of CDIP and CLIP with  $\rho$  at  $M_\infty = 0.6$  and  $\alpha = 0^\circ$  is presented. A "dip" in inlet drag is present in all three methods at  $\rho = 4^\circ$ . The same trend was found in the wind-tunnel data for other values of  $M_\infty$  and  $\alpha$  (ref. 3, p. 33). Inlet lift shows little variation with  $\rho$  from  $-4^\circ$  to  $+4^\circ$ . Some increase in lift coefficient becomes evident for  $\rho > 4^\circ$ .

The preceding four figures have presented a brief overview of relationships of inlet drag and lift with several other parameters: namely,  $A_O/A$ ,  $M_\infty$ ,  $\alpha$ , and  $\rho$ . In general, using the pressure integration technique, the agreement between the flight and wind-tunnel values of CDIP and CLIP was  $\pm 10$  counts and  $\pm 20$  counts or better, respectively.

#### CONCLUDING REMARKS

The NASA Ames Dryden inlet/airframe interaction program has fulfilled its basic objectives. Surface pressure coefficients were measured and matched, wind tunnel to flight. Interaction effects determined from flight and wind-tunnel data have been compared and analyzed for several areas. Wind-tunnel pressure integration techniques for measuring and calculating inlet drags and lifts were successfully adapted to flight testing. Analysis of data taken during the inlet/airframe interaction program has resulted in the following conclusions:

1. In general, most of the flight and wind-tunnel surface pressure coefficients agreed to within  $\pm 0.01$  to  $\pm 0.05$ .
2. Pressure integration techniques and equations used for wind-tunnel testing were successfully employed during the flight-testing program for inlet drag and lift determination.
3. Pressure-integrated values of inlet drag and lift were derived from flight data and verified the wind-tunnel values to within  $\pm 10$  counts or better for inlet drag and to within  $\pm 20$  counts or better for inlet lift.
4. As with the wind-tunnel data, the flight inlet drag from pressure integration did not agree with the wind-tunnel force-balance measurements of drag for certain conditions at a Mach number of  $0.6$ . The difficulty in defining the flow conditions at the inlet entrance plane is the probable cause.

Ames Research Center  
Dryden Flight Research Facility  
National Aeronautics and Space Administration  
Edwards, California, March 4, 1983

## APPENDIX — ERROR ANALYSIS

An increased understanding of the drag and lift data is provided by inclusion of selected segments from the error analysis study performed by McDonnell Aircraft Company for NASA Ames Dryden.

Nineteen flight and wind-tunnel combinations were used as representative conditions to perform the error analysis. Uncertainties in engine airflow, angle of attack, inlet cowl angle, total and static pressures, along with the measurement uncertainties in the pressure transducers, were used in the inlet integration equations for the study. The mathematical model used for the error analysis study can be described as a propagation-of-errors procedure (ref. 13).

For the flight test results, the major contributors to the errors in inlet drag and lift are as follows (in general order of significance): free-stream static pressure, angle of attack, inlet plane total pressure, free-stream total pressure, and engine airflow.

For the results from the AEDC 16-Foot Transonic Wind Tunnel, the major contributors to the errors in inlet drag and lift are as follows (in general order of significance): free-stream static pressure, engine airflow, free-stream total pressure, inlet plane total pressure, and angle of attack.

Most of the trends in the inlet drag and lift levels compare well between flight test and wind-tunnel results, even though the computed uncertainties for the flight test points are about an order of magnitude greater than for the small-scale model data. A representative sample of the trends in inlet drag and lift uncertainties is shown in figure 20. The figure relates  $\pm 2\sigma$  uncertainties in inlet drag and lift as a function of Mach number for  $\alpha = \rho = 0^\circ$ . In this figure and figure 21, the wind-tunnel force-balance data serve as a standard with which the pressure-integrated data are compared. In figure 20(a) the decreasing effect of free-stream static pressure uncertainty (represented by Mach number) on inlet drag is illustrated. Starting with a large  $\pm 2\sigma$  uncertainty at  $M_\infty = 0.6$ , the force-balance and pressure-integrated flight data agree closely at  $M_\infty = 1.5$ . A similar trend for inlet lift is noted in figure 20(b).

Figure 21 illustrates the variation of CDIP and CLIP with angle of attack for  $M_\infty = 0.6$  and  $\rho = 0^\circ$ . Also shown is a  $\pm 2\sigma$  error band associated with an angle-of-attack uncertainty of  $\pm 0.5^\circ$  (assumed for error analysis). The flight and wind-tunnel pressure-integrated drag points agree, but the force-balance-measured inlet drag falls outside of the  $\pm 2\sigma$  uncertainty band for the two higher angles of attack of  $5^\circ$  and  $8^\circ$ , respectively. As with CDIP, the pressure-integrated values of flight and wind-tunnel CLIP data fall well inside the  $\pm 2\sigma$  band. However, just as for CDIP, the force-balance data for CLIP fell outside the uncertainty band at  $\alpha = 5^\circ$  and  $8^\circ$ .

This general agreement indicates that reasonably accurate inlet drag can be obtained by pressure integration methods. It should be noted, however, that careful consideration must be given to the pressure instrumentation locations and to the area assignments.

In summary, the error analysis showed that the uncertainty in the F-15 pressure-integrated inlet drag data from flight-test results ranges from  $\pm 0.0003$  to  $\pm 0.0010$  ( $2\sigma$  in CDIP) compared to  $\pm 0.0007$  for small-scale wind-tunnel test results.

The uncertainty in the F-15 pressure-integrated inlet lift from flight-test results ranges from  $\pm 0.0004$  to  $\pm 0.0022$  ( $2\sigma$  in CLIP) compared to  $\pm 0.0001$  for wind-tunnel test results.

The inlet drag and lift levels and trends obtained from flight tests and wind-tunnel tests compared reasonably well over a wide range of test conditions.

Inlet drag and lift uncertainties increase with altitude and angle of attack; the uncertainties decrease with increasing Mach number and mass flow ratio.

The inlet drag uncertainty can be reduced in flight tests by acquiring data at high dynamic pressure conditions (that is, at minimum allowable altitude for a given flight condition).

For the flight-test results, the free-stream static pressure and angle-of-attack measurements are typically the major contributors to the inlet drag uncertainty. Because of the use of differential pressure transducers, the reference pressure measurement can also become a significant contributor to the pressure-integrated inlet force uncertainty.

Additive (spillage) and lower cowl drag forces are the most significant components of the inlet drag. The uncertainty in the additive drag components is the largest contributor to the total drag uncertainty.

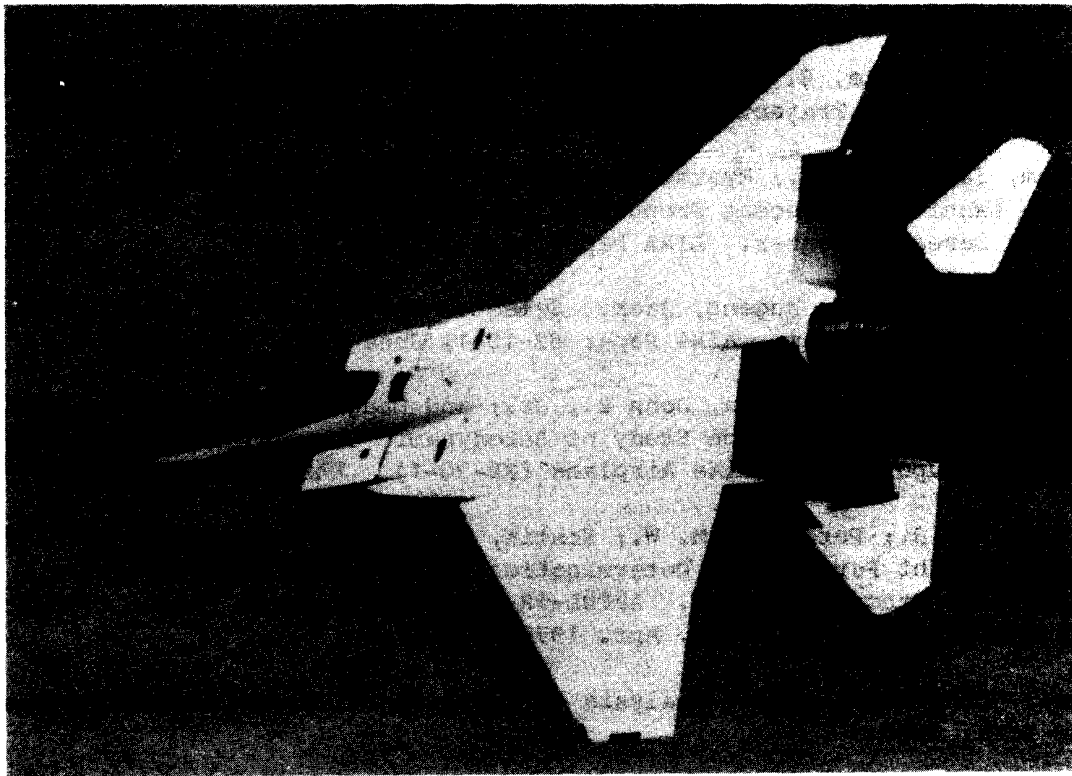
## REFERENCES

1. Smith, Ronald H.: Propulsion-Airframe Interactions Predictability. Performance Predictions Methods, AGARD-CP-242, May 1978, pp. 6-1 to 6-20.
2. Rejeske, J. V.; and Porter, J. L.: Inlet/Aircraft Drag Investigation. AFFDL-TR-74-34, Air Force Flight Dynamics Lab., Wright-Patterson AFB, Ohio, Apr. 1974.
3. Kamman, J. H.; and Wallace, H. W.: Assessment of Installed Inlet Forces and Inlet/Airframe Interactions. AFFDL-TR-76-62, Air Force Flight Dynamics Lab., Wright-Patterson AFB, Ohio, July 1976.
4. Nugent, Jack; Taillon, Norman V.; and Pendergraft, Odis C., Jr.: Status of a Nozzle-Airframe Study of a Highly Maneuverable Fighter. AIAA Paper 78-990, July 1978.
5. Kurtenbach, Frank J.: Comparison of Calculated and Altitude-Facility-Measured Thrust and Airflow of Two Prototype F100 Turbofan Engines. NASA TP-1373, 1978.
6. Webb, Lannie D.; Whitmore, Stephen A.; and Janssen, Randall L.: Preliminary Flight and Wind Tunnel Comparisons of the Inlet/Airframe Interaction of the F-15 Airplane. AIAA Paper 79-0102, Jan. 1979.
7. Schweikhard, William G.: Test Techniques, Instrumentation, and Data Processing. Distortion Induced Engine Instability, AGARD-LS-72, Nov. 1974, pp. 6-1 to 6-43.
8. Swann, M. R.; Duke, E. L.; Enevoldson, E. K.; and Wolfe, T. D.: Experience with Flight Test Trajectory Guidance. AIAA Paper 81-2504, Nov. 1981.
9. Burcham, Frank W., Jr.; Myers, Lawrence P.; Nugent, Jack; Lasagna, Paul L.; and Webb, Lannie D.: Recent Propulsion System Flight Tests at the NASA Dryden Flight Research Center. AIAA Paper 81-2438, Nov. 1981.
10. Webb, Lannie D.; and Nugent, Jack: Selected Results of the F-15 Propulsion Interactions Program. AIAA Paper 82-1041, June 1982.
11. Arnaiz, Henry H.; Peterson, John B., Jr.; and Daugherty, James C.: Wind-Tunnel/Flight Correlation Study of Aerodynamic Characteristics of a Large Flexible Supersonic Cruise Airplane (XB-70-1). NASA TP-1516, 1980.
12. Schoelen, F. J.; Petersen, M. W.; Kostin, L. C.; and Gilbertson, M.: Inlet/Nozzle Flight Performance Determination (Wind Tunnel Test Program). Volume I - Program Results. AFFDL-TR-78-173, Air Force Flight Dynamics Lab., Wright-Patterson AFB, Ohio, Apr. 1979.
13. Mandel, John: Statistical Analysis of Experimental Data. John Wiley and Sons, New York, 1967.

TABLE 1. - COMPARISON OF ACCURACIES FOR THREE MEASUREMENT SOURCES

Technique (source)	$M_\infty$	$\alpha$ , deg	$C_p$	CDIP	CLIP
Pressure integration (flight)	0.6 to 1.5	0° to 8°	$\pm 0.01$ to $\pm 0.05^a$	$\pm 3 \times 10^{-4}$ to $\pm 10 \times 10^{-4}$	$\pm 4 \times 10^{-4}$ to $\pm 22 \times 10^{-4}$
Pressure integration (wind tunnel)	0.6 to 1.5	0° to 5°	---	$\pm 0.7 \times 10^{-4}$	$\pm 1 \times 10^{-4}$
Force balance (wind tunnel, ref. 3)	0.9	5°	0.005	$\pm 3 \times 10^{-4}$	$\pm 6 \times 10^{-4}$

<sup>a</sup>An uncertainty of  $\pm 0.006$  for  $M_\infty$  at subsonic speeds (from airspeed calibration runs), root-mean-square (rms) errors from laboratory temperature calibrations of the pressure transducers, reference tank errors, and pcm, including errors, were used. The appendix discusses in greater detail the uncertainties in inlet drag and lift.



ECN 9325

Figure 1. F-15 airplane in flight.



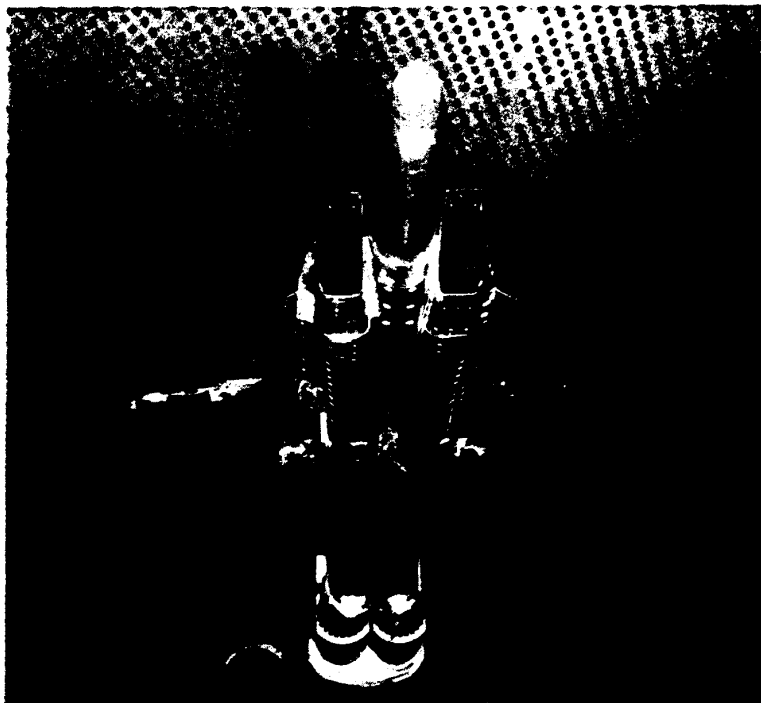
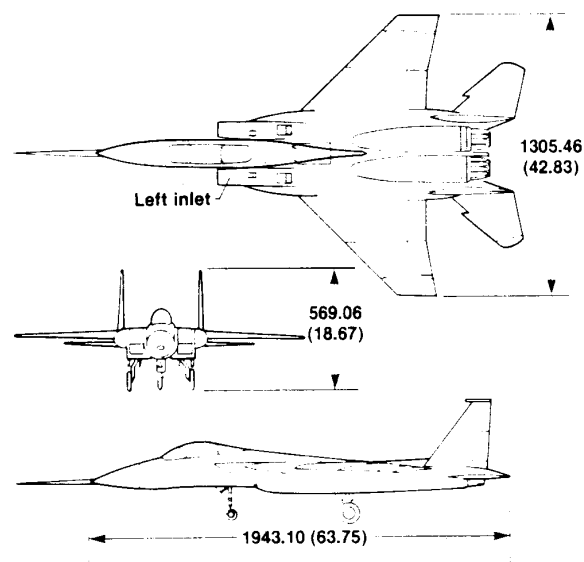
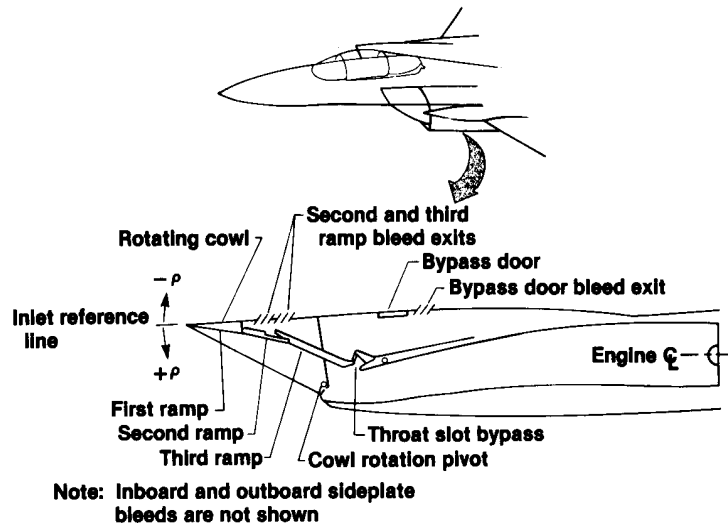


Figure 2. Small-scale (7.5-percent) inlet model in AEDC 16-Foot Transonic Wind Tunnel.

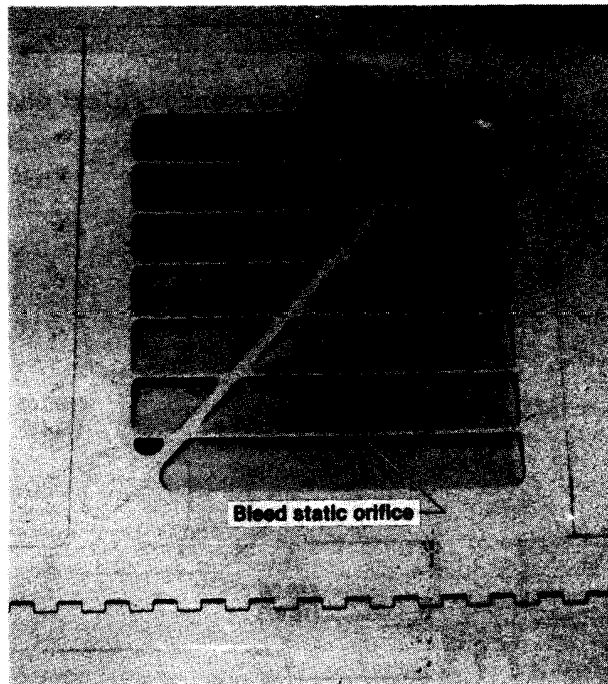


(a) Three-view drawing. Dimensions are in centimeters (feet).

Figure 3. F-15 airplane and inlet.



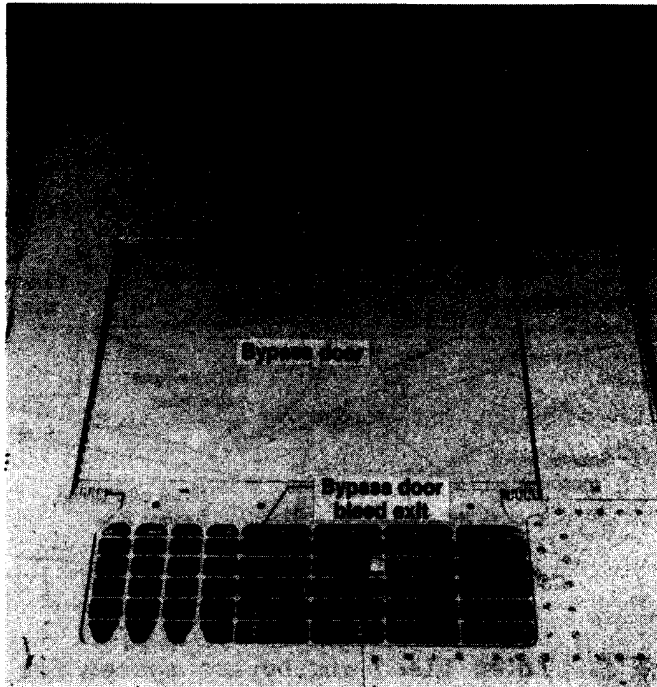
(b) Ramps, bleed exits, and bypass door exits.



E 34013

(c) Second and third ramp bleed exits.

Figure 3. Continued.



E 35054

(d) Bypass door bleed exits.

Figure 3. Concluded.

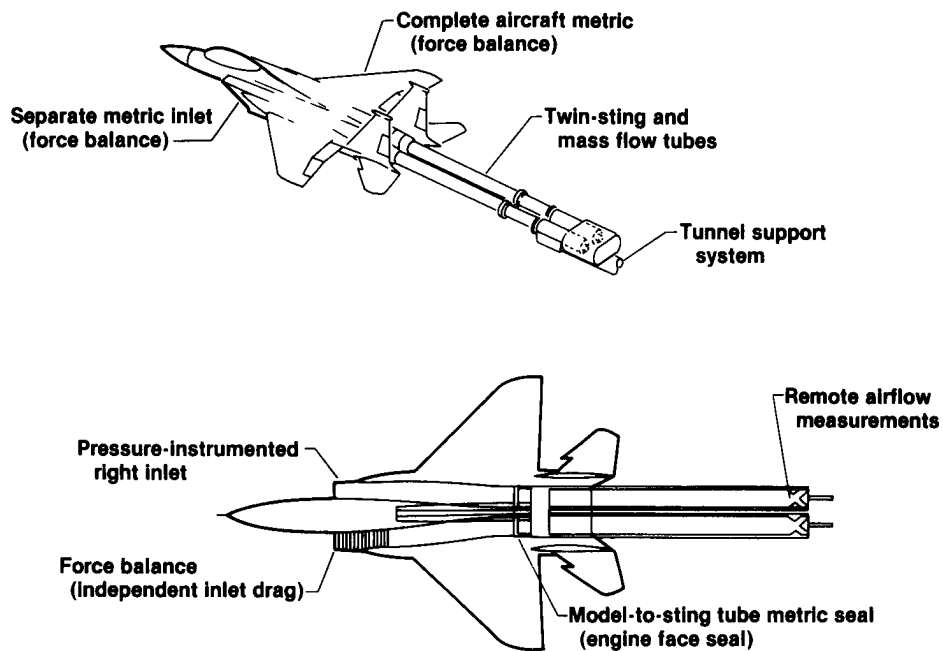


Figure 4. Inlet model twin force-balance sting system.

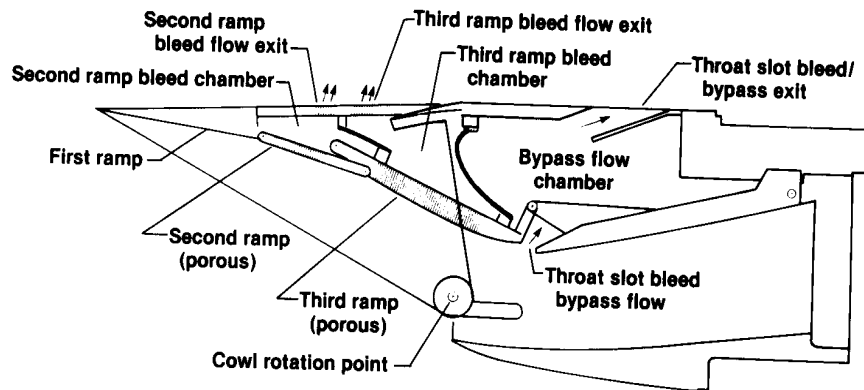
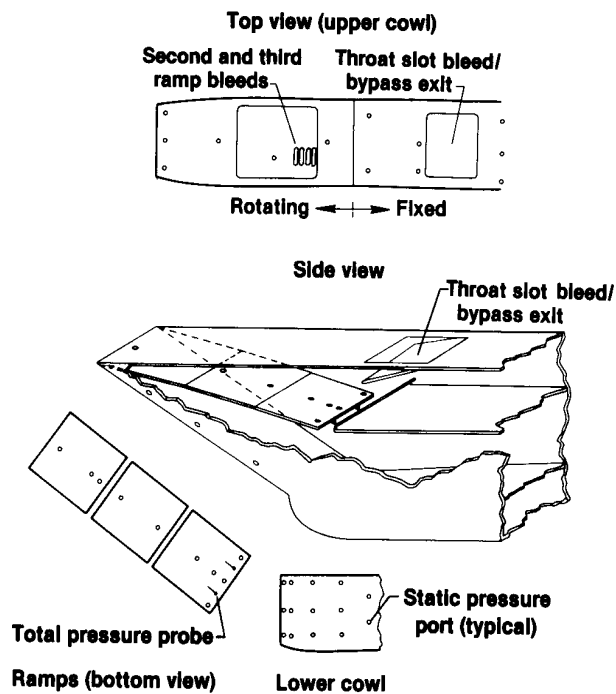
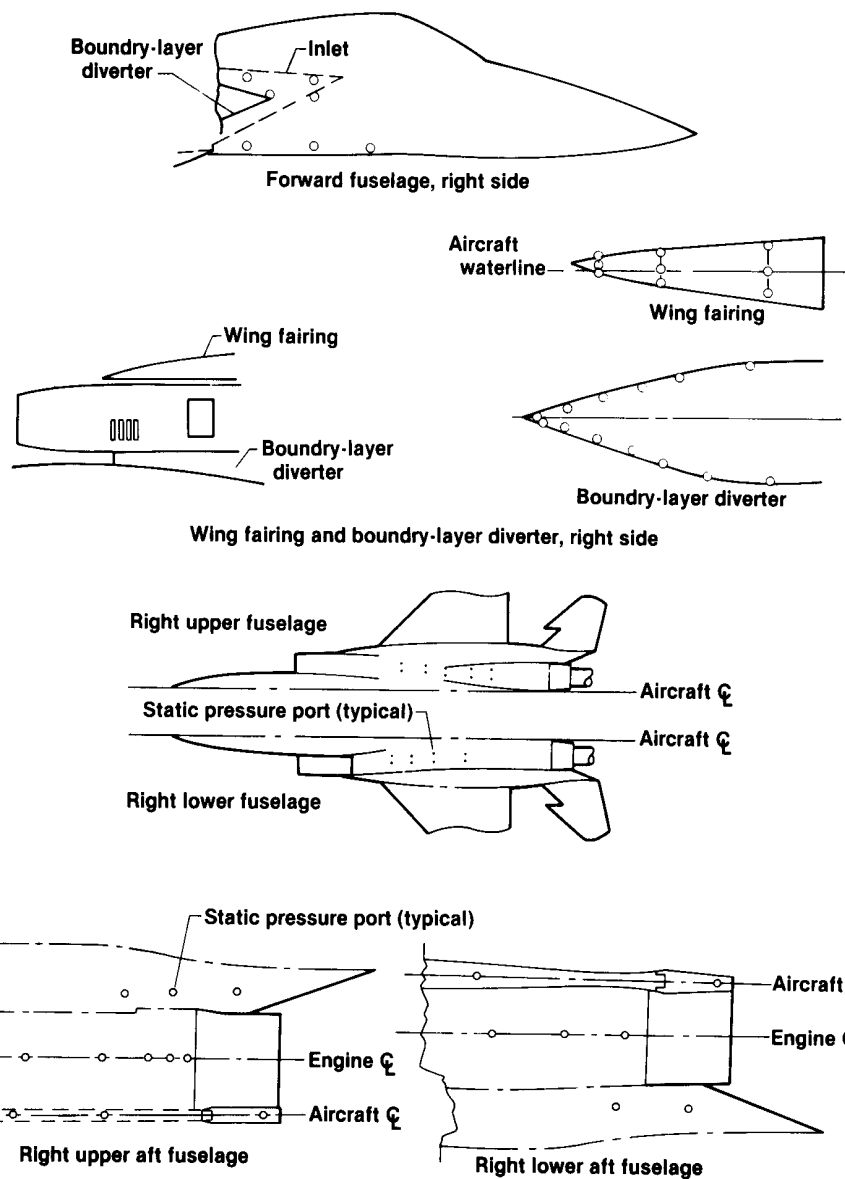


Figure 5. Inlet bleed and bypass system for wind-tunnel model.



(a) Inlet pressures.

Figure 6. Static pressure ports on the 7.5-percent wind-tunnel model.



(b) Fuselage, wing fairing, and boundary-layer diverter pressures.

Figure 6. Concluded.

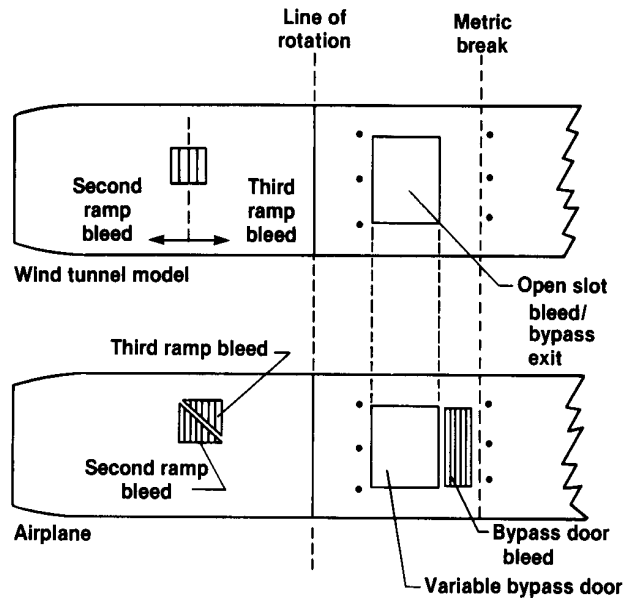


Figure 7. Comparison of airplane and wind-tunnel model bleed and bypass systems on the upper cowl.

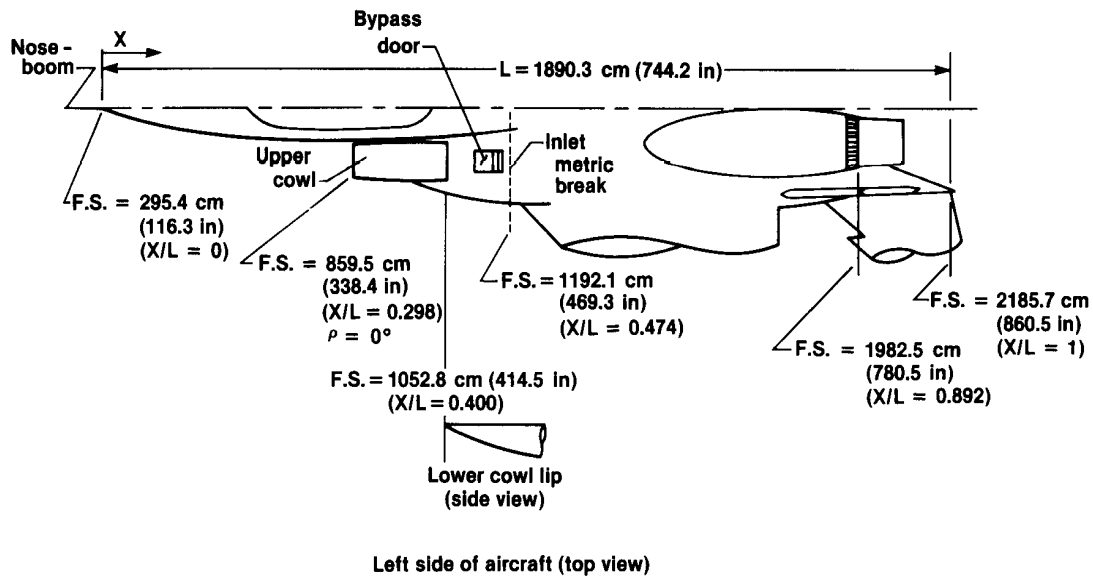


Figure 8. Major reference points for F-15 aircraft and wind-tunnel model.

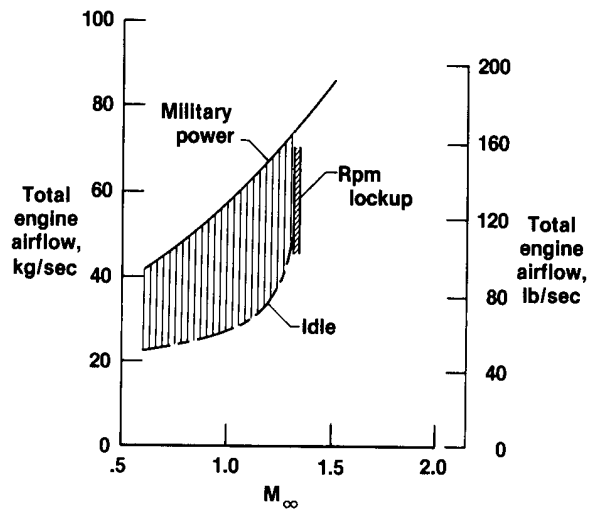


Figure 9. Total engine airflow for the F-100-PW-100 afterburning turbofan engine at an altitude of 9.1 km (30,000 ft).

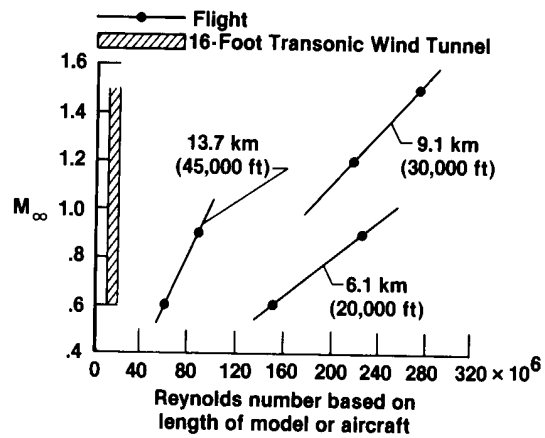
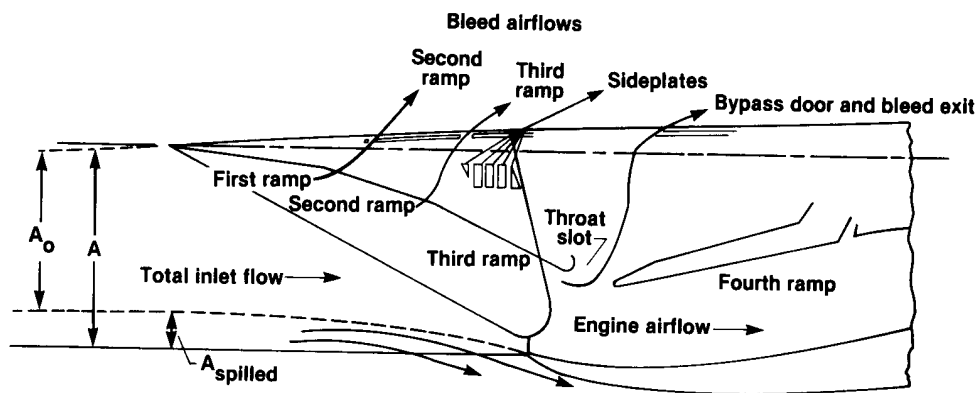


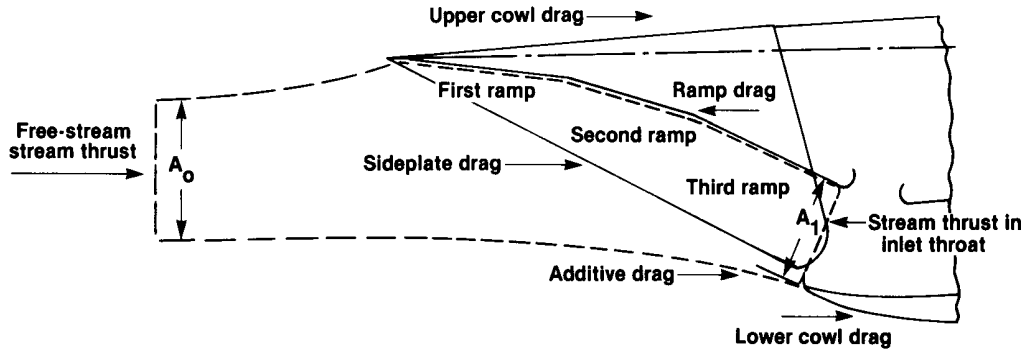
Figure 10. Flight and wind-tunnel Reynolds numbers.



$$A_0 = \Sigma (\text{Bleed airflows}) + \text{Engine airflow}$$

(a) Diagram showing sum of inlet captured stream tube area ( $A_0$ ) and geometric capture area ( $A$ ).

Figure 11. General terms for pressure-integrated inlet drags and inlet capture ratios.

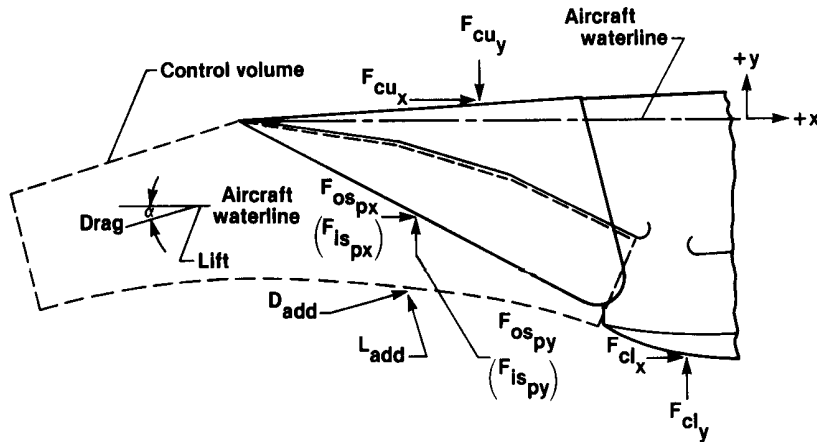


$$\text{Inlet drag} = \text{additive drag} + \text{upper cowl drag} + \text{lower cowl drag} + \text{sideplate drag}$$

where

$$\text{additive drag} = \text{drag on three ramps} + \text{stream thrust in inlet throat} - \text{free-stream stream thrust}$$

(b) Relationships used in the calculation of pressure-integrated inlet drag.



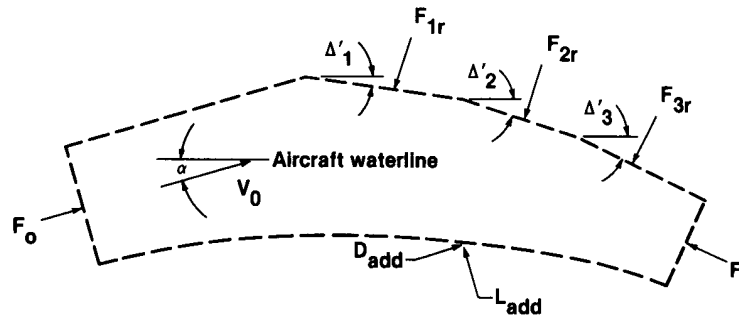
$$\text{Inlet drag} = D_{\text{add}} + \left( F_{\text{cu}_x} + F_{\text{cl}_x} + F_{\text{os}_{px}} + F_{\text{is}_{px}} \right) \cos \alpha + \left( -F_{\text{cu}_y} + F_{\text{cl}_y} + F_{\text{os}_{py}} + F_{\text{is}_{py}} \right) \sin \alpha$$

$$\text{Inlet lift} = L_{\text{add}} - \left( F_{\text{cu}_x} + F_{\text{cl}_x} + F_{\text{os}_{px}} + F_{\text{is}_{px}} \right) \sin \alpha + \left( -F_{\text{cu}_y} + F_{\text{cl}_y} + F_{\text{os}_{py}} + F_{\text{is}_{py}} \right) \cos \alpha$$

(c) Details of inlet drag and lift equations.

Figure 11. Continued.



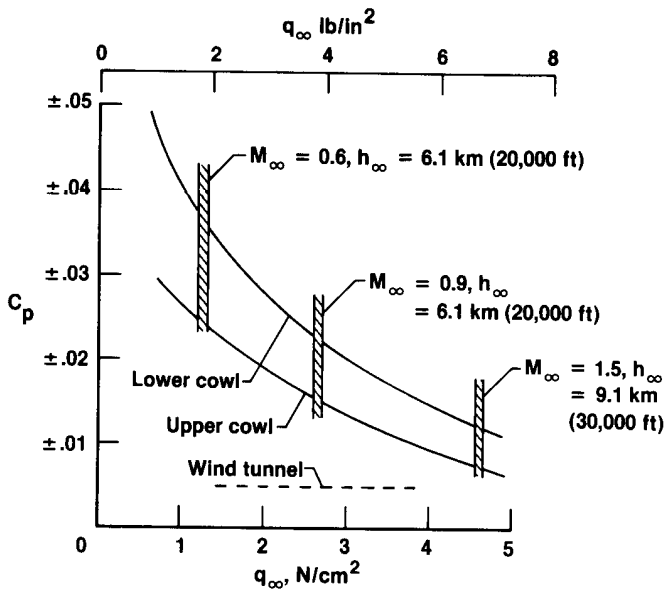


$$D_{add} = F_{1r} \sin (\alpha + \Delta'_1) + F_{2r} \sin (\alpha + \Delta'_2) + F_{3r} \sin (\alpha + \Delta'_3) + F_1 \cos (\alpha + \Delta'_3) - F_0$$

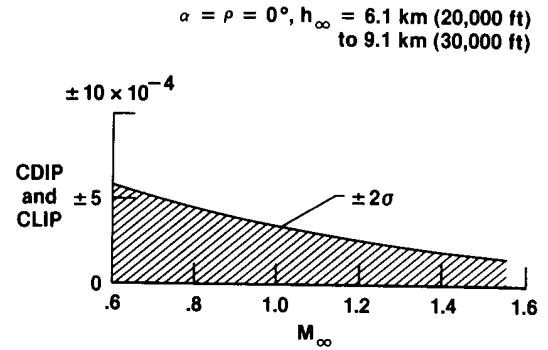
$$L_{add} = F_{1r} \cos (\alpha + \Delta'_1) + F_{2r} \cos (\alpha + \Delta'_2) + F_{3r} \cos (\alpha + \Delta'_3) - F_1 \sin (\alpha + \Delta'_3)$$

(d) Additive drag and lift relationships for the control volume shown in figure 11(c).

Figure 11. Concluded.

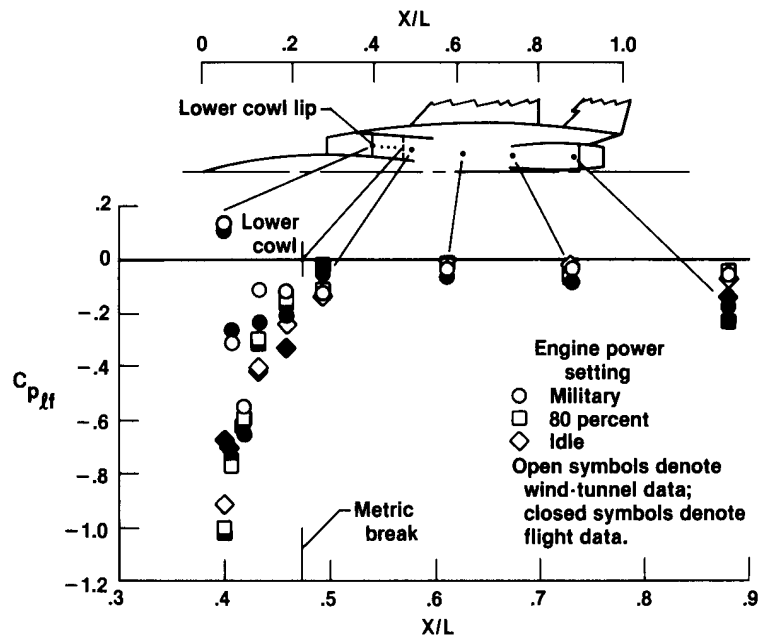


(a) Uncertainties in  $C_p$ .

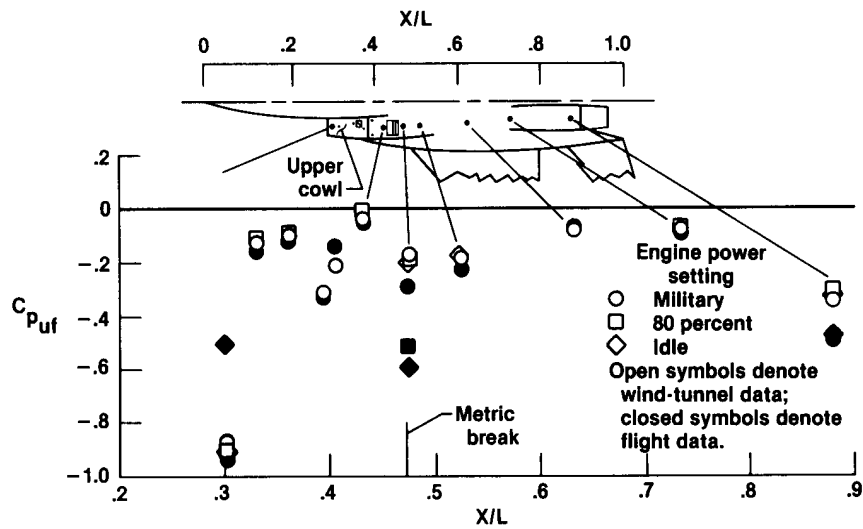


(b) Uncertainties in flight CDIP and CLIP.

Figure 12. Uncertainties in  $C_p$ , CDIP, and CLIP for various Mach numbers and altitudes.

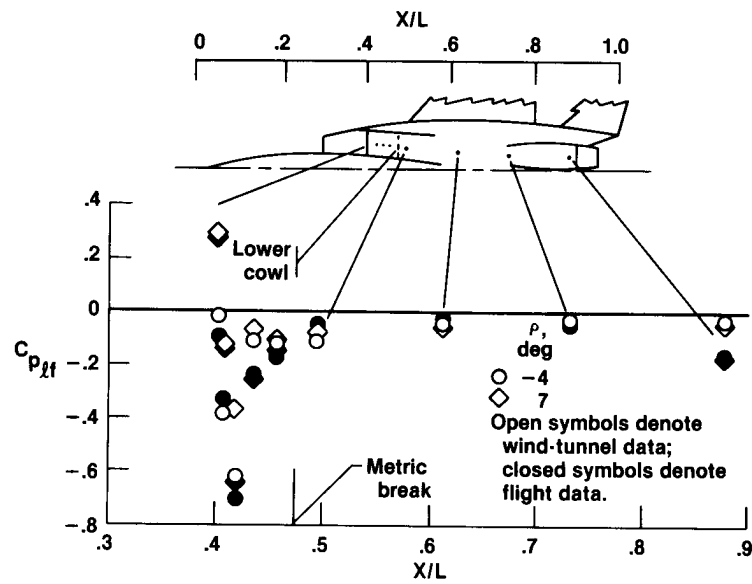


(a) Lower surface.

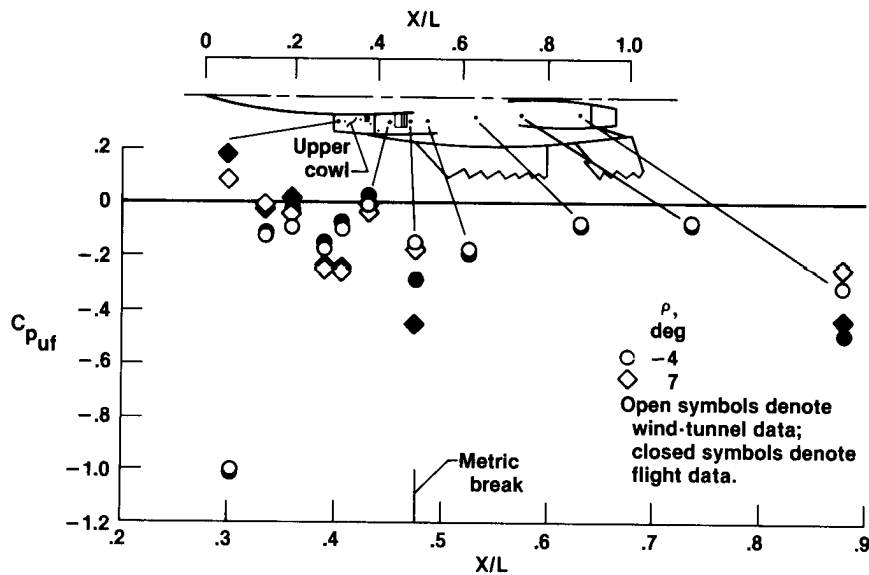


(b) Upper surface.

Figure 13. Effects of mass flow on upper and lower surface pressures at  $M_\infty = 0.9$ ,  $\alpha = 3^\circ$ , and  $\rho = 0^\circ$ .

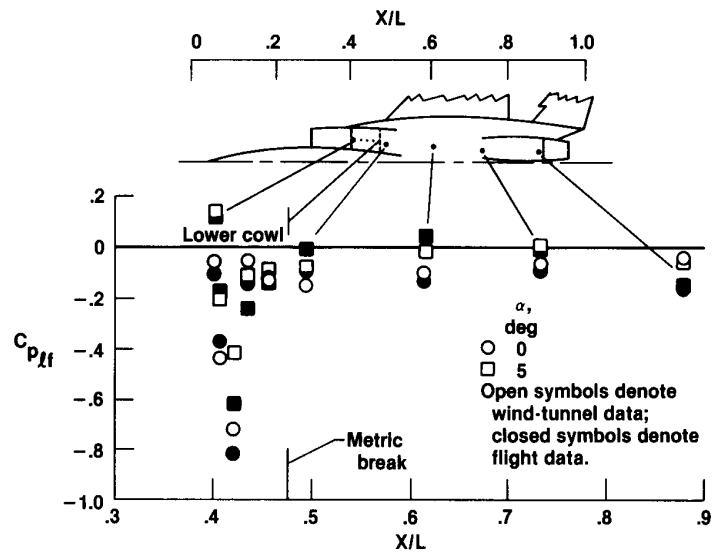


(a) Lower surface.

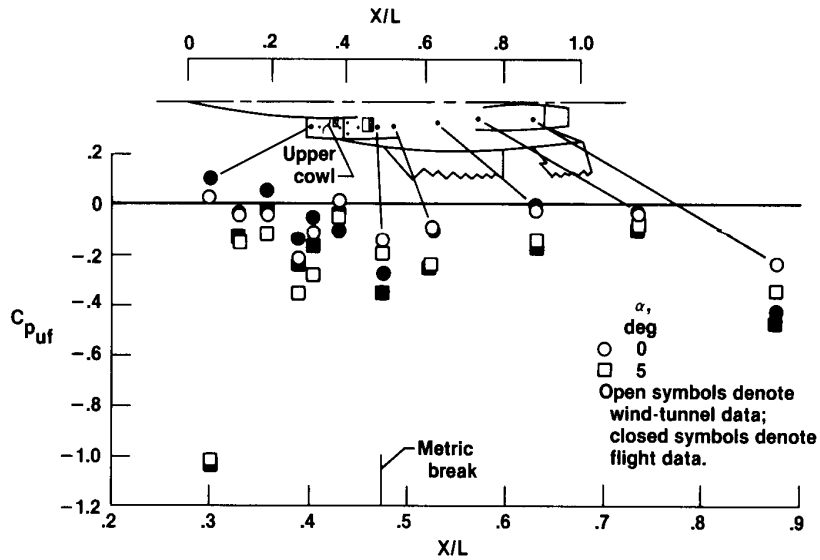


(b) Upper surface.

Figure 14. Effect of variable cowl on pressures over the upper and lower surfaces of the aircraft at  $M_\infty = 0.9$ ,  $\alpha = 3^\circ$ , and military power.

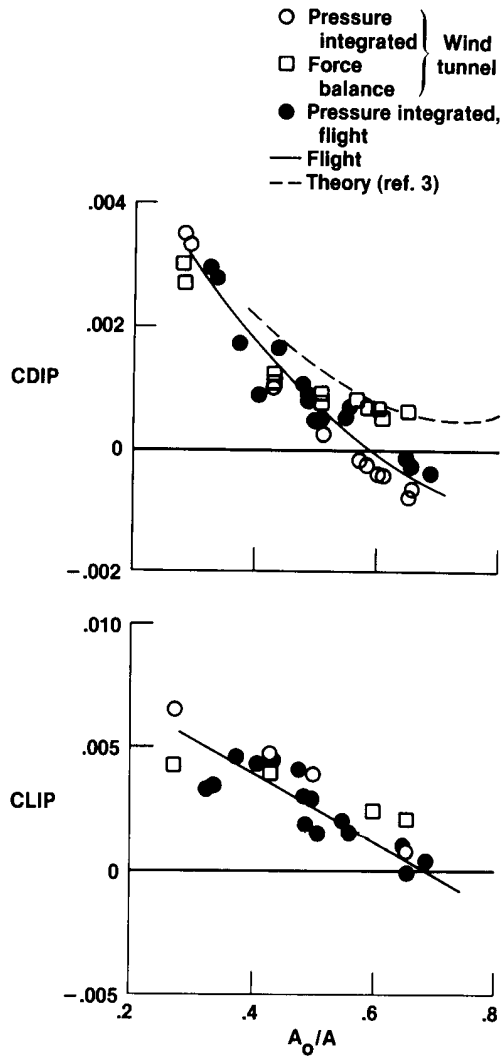


(a) Lower surface.

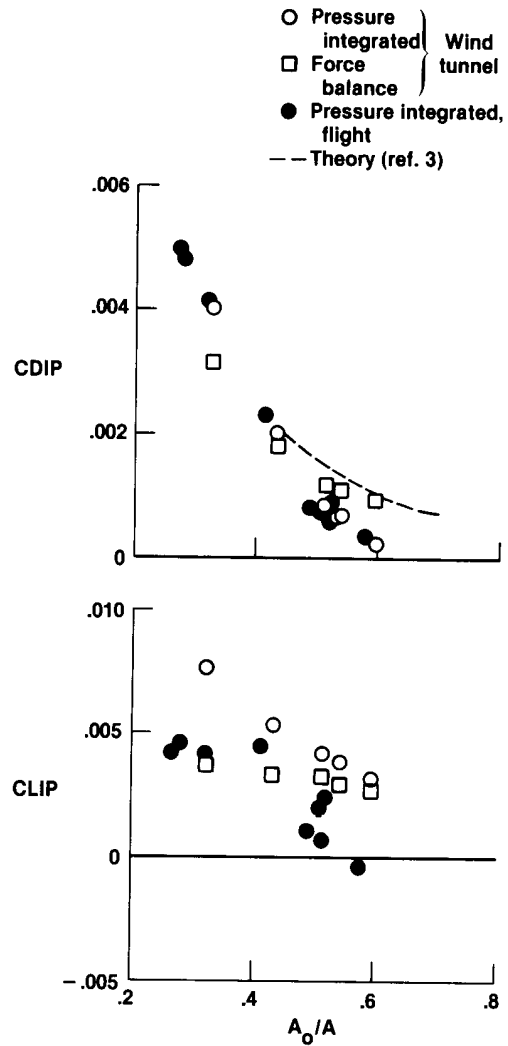


(b) Upper surface.

Figure 15. Variation of surface pressure coefficients with  $X/L$  for two angle of attack at  $M_\infty = 0.9$ ,  $\rho = 0^\circ$ , and military power.

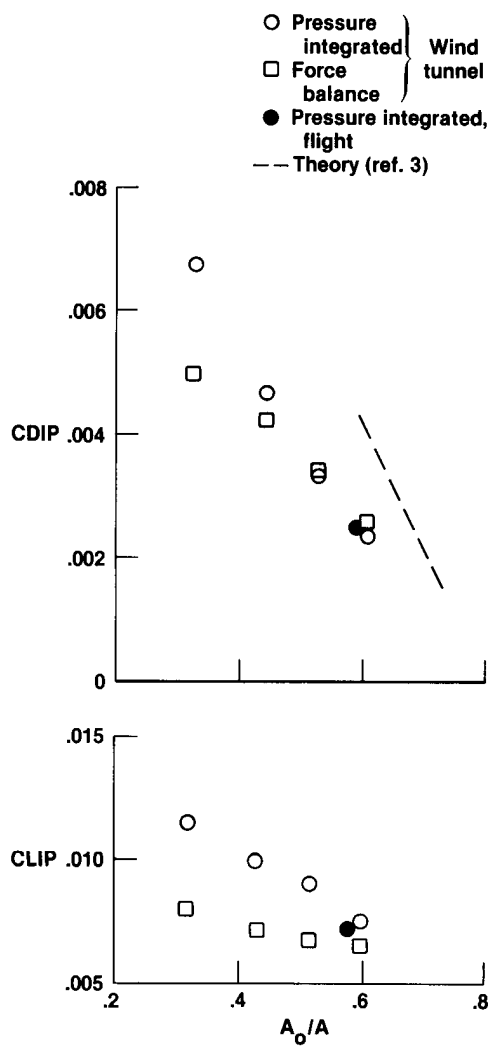


(a)  $M_\infty = 0.6$ ,  $\alpha = 0^\circ$ .

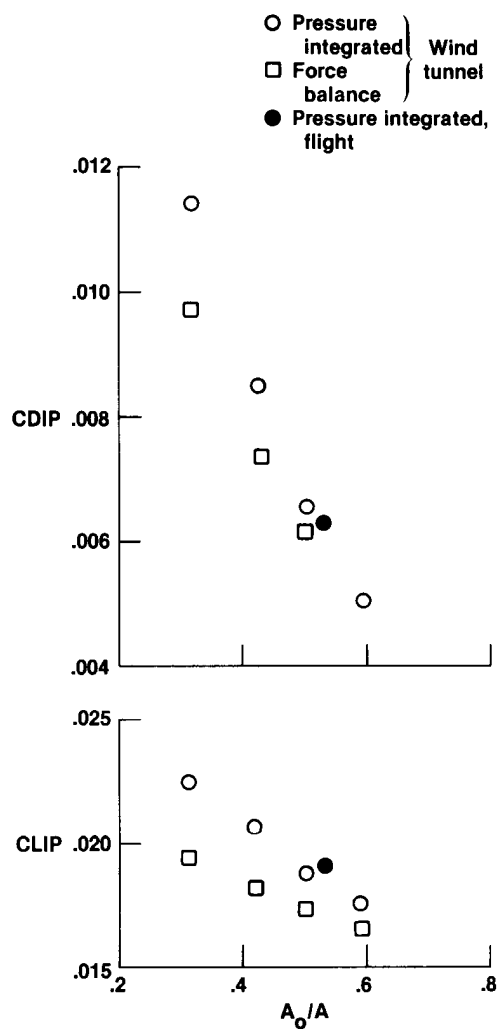


(b)  $M_\infty = 0.9$ ,  $\alpha = 0^\circ$ .

Figure 16. Variation of  $CDIP$  and  $CLIP$  with  $A_O/A$  for  $\rho = 0^\circ$ ,  $\Delta'_3 = 11.2^\circ$ , and  $\beta = 0^\circ$ .



(c)  $M_\infty = 1.2$ ,  $\alpha = 0^\circ$ .



(d)  $M_\infty = 1.5$ ,  $\alpha = 5^\circ$ .

Figure 16. Concluded.

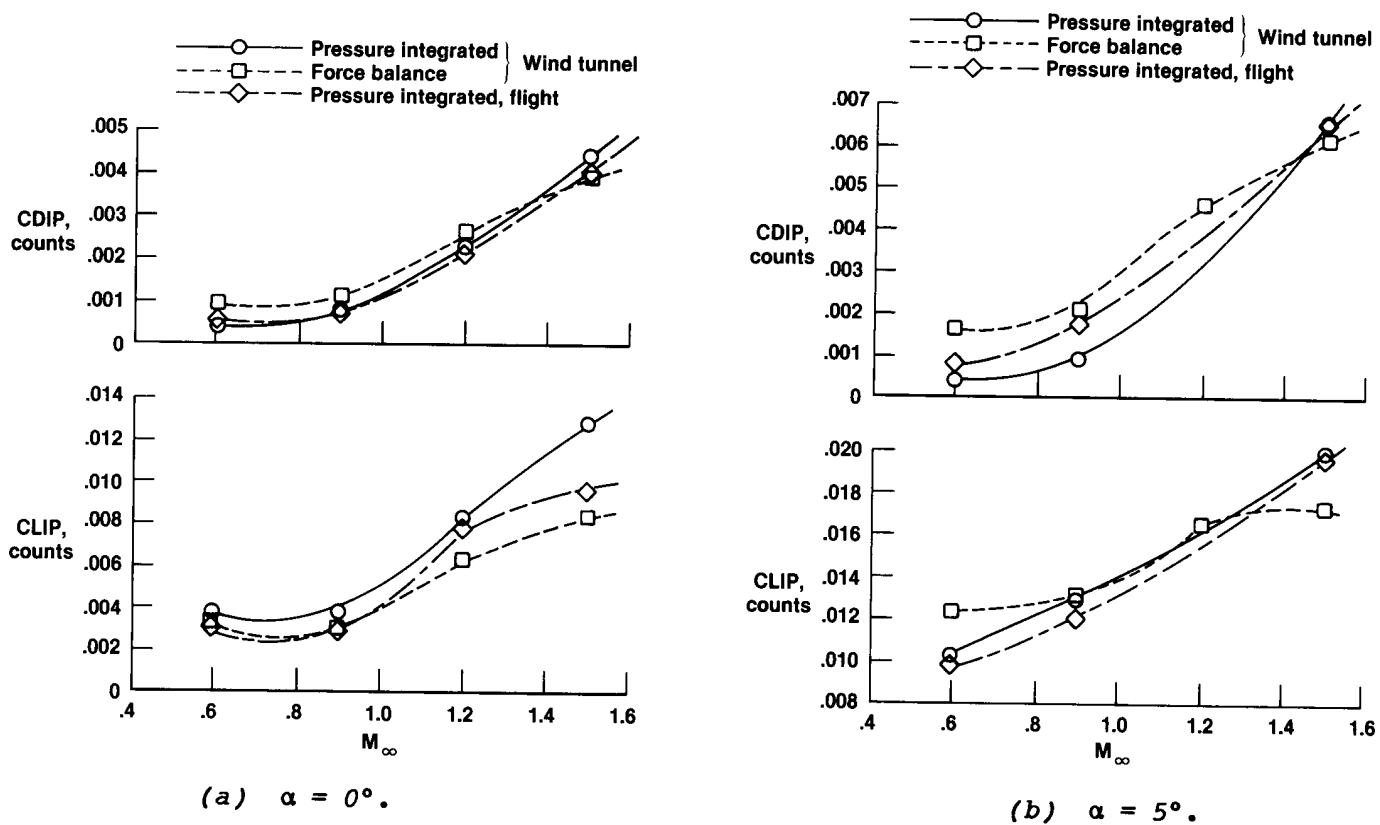


Figure 17. Variation of  $CDIP$  and  $CLIP$  with  $M_\infty$  for two angles of attack at  $\rho = 0^\circ$ .

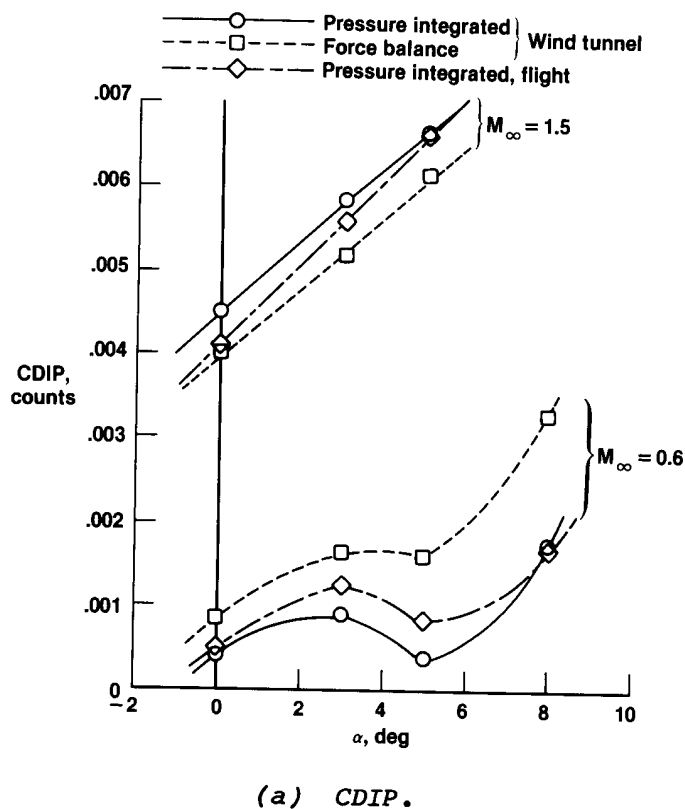
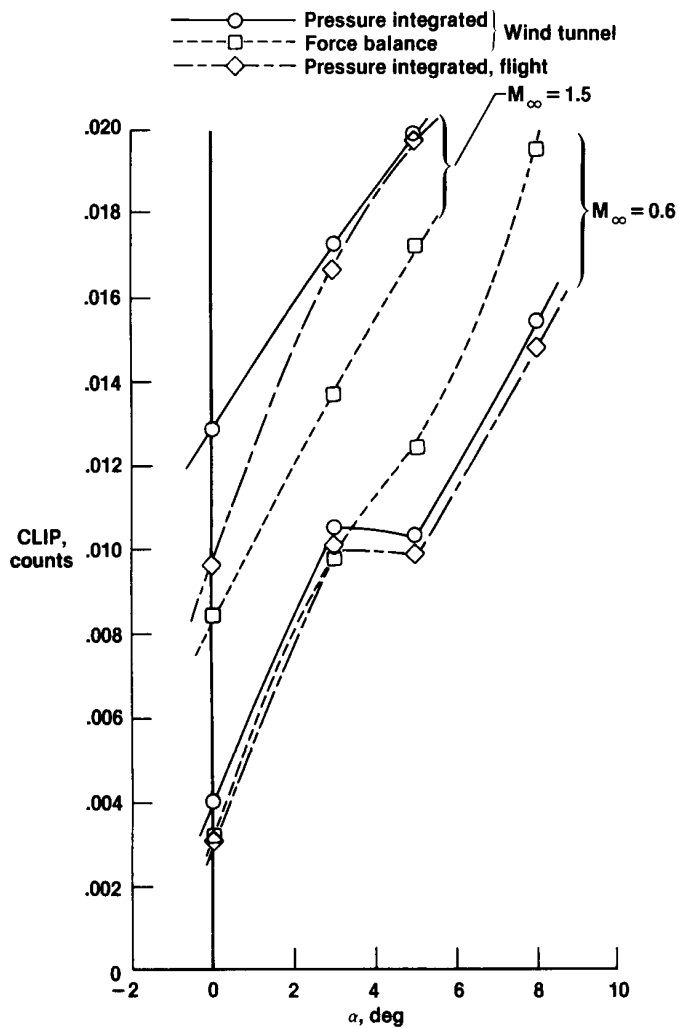


Figure 18. Effect of  $\alpha$  on  $CDIP$  and  $CLIP$ ;  $\rho = 0^\circ$ .



(b) CLIP.

Figure 18. Concluded.

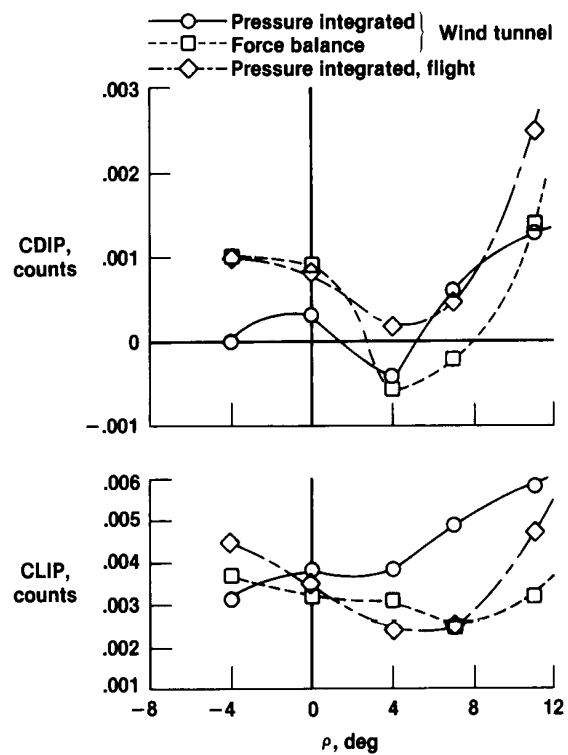
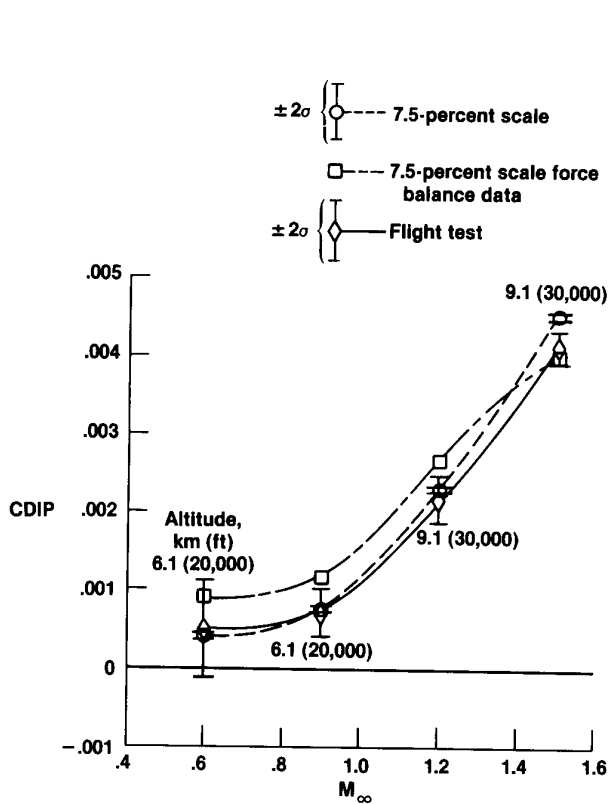
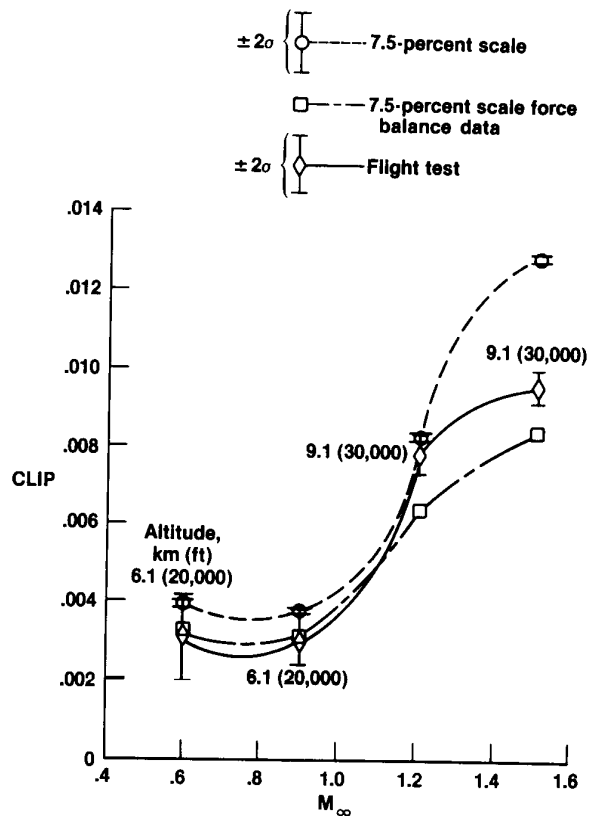


Figure 19. Effect of  $\rho$  on CDIP and CLIP at  $M_\infty = 0.6$  and  $\alpha = 0^\circ$ .



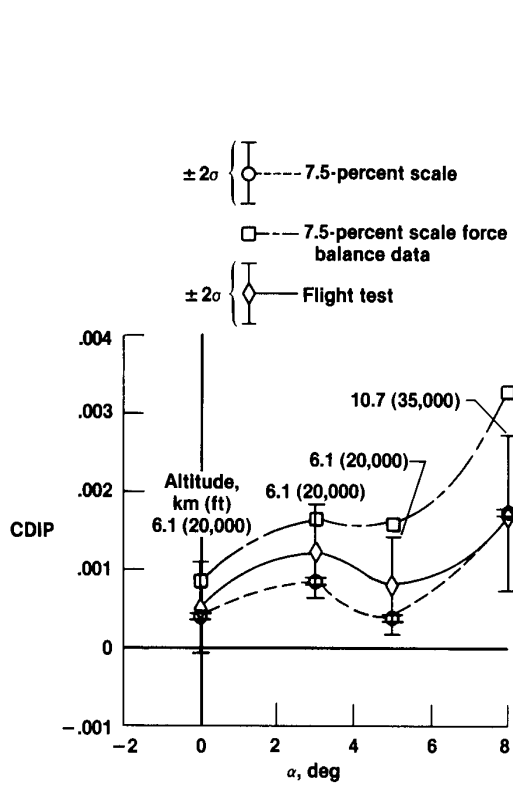


(a) Variation of inlet drag with Mach number.

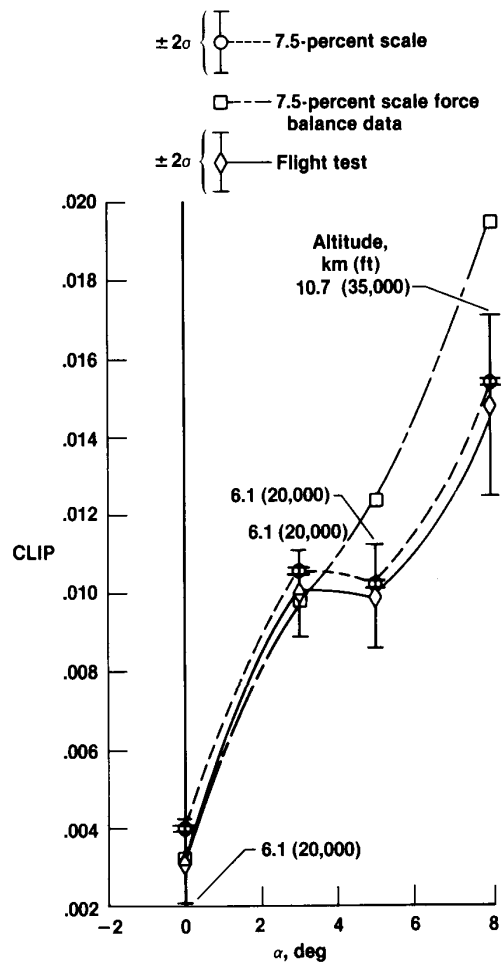


(b) Variation of inlet lift with Mach number.

Figure 20. Variation of inlet drag and lift uncertainties with Mach number for  $\alpha$  and  $\rho = 0^\circ$ .



(a) Angle of attack as a function of inlet drag coefficient;  $M_\infty = 0.6$ ,  $\rho = 0^\circ$ .



(b) Angle of attack as a function of inlet lift coefficient;  $M_\infty = 0.6$ ,  $\rho = 0^\circ$ .

Figure 21. Effect of angle of attack on inlet lift and drag coefficients and the uncertainty in the data.

[illegible]

\*For sale by the National Technical Information Service, Springfield, Virginia 22161.